

Pressure-driven wrinkling of soft inner-lined tubes

Benjamin Foster

E-mail: ben_foster@berkeley.edu
Physics Department, University of California at Berkeley, Berkeley, California
94720, USA

Nicolás Verschueren

E-mail: nverschueren@berkeley.edu
Physics Department, University of California at Berkeley, Berkeley, California
94720, USA

Edgar Knobloch

E-mail: knobloch@berkeley.edu
Physics Department, University of California at Berkeley, Berkeley, California
94720, USA

Leonardo Gordillo

E-mail: leonardo.gordillo@usach.cl
Departamento de Física, Facultad de Ciencia, Universidad de Santiago de Chile,
Chile

Abstract. A simple equation modelling an inextensible elastic lining of an inner-lined tube subject to an imposed pressure difference is derived from a consideration of the idealised elastic properties of the lining and the pressure and soft-substrate forces. Two cases are considered in detail, one with prominent wrinkling and a second one in which wrinkling is absent and only buckling remains. Bifurcation diagrams are computed via numerical continuation for both cases. Wrinkling, buckling, folding, and mixed-mode solutions are found and organised according to system-response measures including tension, in-plane compression, maximum curvature and energy. Approximate wrinkle solutions are constructed using weakly nonlinear theory, in excellent agreement with numerics. Our approach explains how the wavelength of the wrinkles is selected as a function of the parameters in compressed wrinkling systems and shows how localised folds and mixed-mode states form in secondary bifurcations from wrinkled states. Our model aims to capture the wrinkling response of arterial endothelium to blood pressure changes but applies much more broadly.

Keywords: Nonlinear elastica; wrinkling; buckling; bifurcation

Submitted to: *New J. Phys.*

1. Introduction

Lateral compression of a finite thin floating elastic sheet generates periodic wrinkles whose wavelength is the result of a balance between elastic forces and the restoring weight of the entrained liquid. On further compression, the sheet undergoes a transition from the wrinkled state to one characterised by a single fold [1]. However, wrinkling is not exclusive to floating elastica: the weight of the liquid can be replaced by other forces and used to generate wrinkling in both two-dimensional circular and three-dimensional spherical and curved geometries. Examples are provided by laterally compressed [2] or curved bilayer materials [3], as well as vertically loaded floating circular sheets [4, 5, 6] and spring-loaded interfaces [7]. In contrast, compressed or deflated spherical shells [8, 9] exhibit buckling with no preferred length scale, as do elastic rings supporting a soap film [10, 11, 12, 13]. Constrained buckling of elastic rings exhibits similar properties [14].

Understanding how surfaces wrinkle and then fold in different geometries under specific forces usually requires solving complicated systems of partial differential equations. The thin floating sheet in one dimension (1D) provides an exception. This system is not only modelled by a simple equation for in-plane deformations, but also turns out to be completely integrable in the limit of infinite extent [15, 16, 17, 18, 19]. As a result the remarkable shapes of both wrinkles and folds on thin floating sheets can be described using stunningly simple mathematical expressions [16, 17], which naturally implies closed formulas for the wrinkling/folding thresholds in parameter space.

In this article we study the competition between in-plane wrinkling and buckling in a circular geometry within a similar framework. The results lead to greater understanding of a number of different systems where such competition is present. These include in-plane wrinkling of the elastic lining of an artery where wrinkled-to-unwrinkled cycles driven by diastolic-to-systolic blood pressure changes may prevent clogging and adhesion of platelets via large changes in the local curvature of its endothelium [20, 21]. Such cycling is likely to prove useful in other applications. A similar wrinkling instability is present in a rotating Hele-Shaw cell when a higher density fluid in the center is separated from a lower density fluid on the outside by an elastic membrane [22, 23, 24].

We construct an idealised two-dimensional model for this class of systems and compute strongly deformed states up to the point of self-contact, analyse their stability, and organise the results in the form of bifurcation diagrams. These diagrams describe the response of the system (compression, tension, maximum curvature) as a function of a control parameter, for example, the imposed pressure difference. We use the results to identify a transition from unwrinkled to periodic wrinkled states and then to folded states similar to what is observed in spring-loaded linings or tubular chitosan hydrogel surfaces [7, 25]. Fold states arise via secondary bifurcations from the wrinkled state as in the one-dimensional case. Two cases are considered in detail, one with prominent wrinkling and a second one in which wrinkling is absent and only buckling remains.

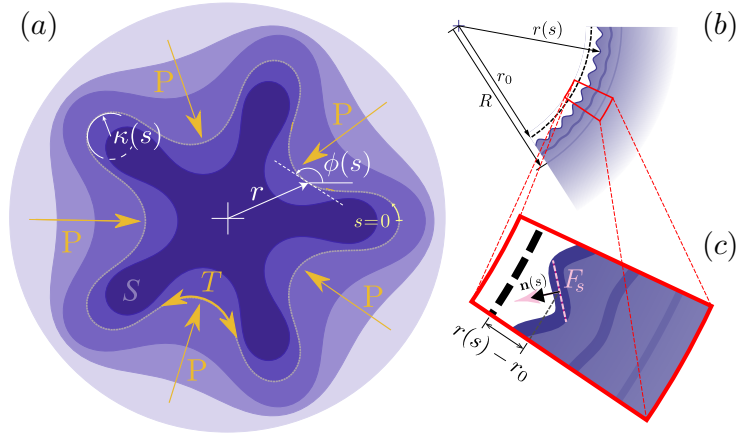


Figure 1. (a) Schematic view of a tube undergoing pressure-driven wrinkling with wavenumber $m = 5$. (b,c) Force exerted on the lining by the exterior substrate.

2. The Model

To represent the lining on the inside of a soft tube, we consider an inextensible, infinitely thin membrane of length $L = 2\pi R$ attached to a soft substrate as shown in figure 1. We suppose that in equilibrium ($P = 0$) the unlined soft tube has an inner radius $r_0 < R$ (figure 1(b)) and hence that, when lined, the lining is forced to wrinkle. We model this force by an inward normal force per unit area $\mathbf{F}_s = \frac{1}{2}K(r(s)^2 - r_0^2)\mathbf{n}(s)$ (figure 1(c)). Here $r = r(s)$ denotes the lining profile (r is the distance from the tube centre) and s is the arclength. The substrate force \mathbf{F}_s is the simplest nonlinear model that is differentiable at $r = 0$ and that behaves like the classical Winkler foundation [26] when expanded around r_0 , with constant stiffness $k = Kr_0$. Moreover, the quadratic contribution to the force vanishes in the flat-foundation limit, i.e. as $r_0 \rightarrow \infty$, again recovering a Winkler-type foundation response. Although higher-order models [27], and in particular models that include nonlocal contributions [2], may provide a more realistic representation of the substrate forces, the Winkler model has been used extensively in studies of substrate-supported elastica and has provided important insights into the instabilities responsible for both wrinkled and localised states [7, 28, 29].

For in-plane deformations the resulting system is then described by

$$\mathcal{B} \left(\frac{1}{2}\kappa^3 + \partial_s^2 \kappa \right) - T\kappa - P + \frac{1}{2}K(r_0^2 - r^2) = 0, \quad (1)$$

where $\kappa \equiv \partial_s \phi$ is the local curvature. Here ϕ is the angle between the tangent plane and the horizontal or x -axis (figure 1(a)). In terms of Cartesian coordinates (x, y) with origin at the tube center, $\partial_s x = \cos \phi$, $\partial_s y = \sin \phi$ and $r^2 \equiv x^2 + y^2$. The constants in (1) are the bending modulus \mathcal{B} and the (unknown) tension T required to maintain the length L of the lining ($T < 0$ implies tangential compression). A brief derivation of (1) similar to that in [12] can be found in Appendix A. In the following we absorb the constant term $\frac{1}{2}Kr_0^2$ in the pressure P . The resulting system is then similar to a rotating Hele-Shaw cell filled with two fluids separated by an elastic membrane, with a higher density interior [22, 23, 24].

We define the natural length scale

$$\lambda \equiv \left(\frac{\mathcal{B}}{K} \right)^{\frac{1}{5}}, \quad (2)$$

and introduce a dimensionless parameter that measures the perimeter of the lining in terms of λ , $\ell \equiv R/\lambda$. We scale (1) according to $s \sim R$, $\kappa \sim R^{-1}$, $r \sim R$, $T \sim \mathcal{B}/R^2$, $P \sim \mathcal{B}/R^3$, yielding

$$\partial_s^3 \phi + \frac{1}{2} (\partial_s \phi)^3 - T \partial_s \phi - P - \frac{1}{2} \ell^5 r^2 = 0. \quad (3)$$

The area within the lining, scaled relative to the area of the circle, is conveniently written via Stokes theorem as

$$S = \frac{1}{2\pi} \oint [x \sin \phi - y \cos \phi] ds, \quad (4)$$

and, accordingly, its compression is $\Delta \equiv 1 - S$. The total energy, also scaled relative to the circle, is given by

$$E = \frac{2}{\pi(4 + \ell^5)} \oint \left[(\partial_s \phi)^2 + \frac{1}{4} \ell^5 r^2 (x \sin \phi - y \cos \phi) \right] ds. \quad (5)$$

3. Linear and weakly nonlinear theory

The simplest solution to (3) is the circle:

$$\phi_0(s) = s + \pi/2, \quad x_0(s) = \cos s, \quad y_0(s) = \sin s. \quad (6)$$

This solution requires a simple relationship between the imposed pressure and the resulting tension,

$$T_0 = \frac{1}{2} (1 - \ell^5) - P_0, \quad (7)$$

and serves as the starting point (order zero) for linear and weakly nonlinear analysis. Introducing a small parameter ϵ measuring the amplitude of a perturbation of the circle solution, we expand ϕ , x , y , T and P as follows:

$$\begin{aligned} \phi(s) &= \sum_{j=0}^N \epsilon^j \phi_j(s), & x(s) &= \sum_{j=0}^N \epsilon^j x_j(s), & y(s) &= \sum_{j=0}^N \epsilon^j y_j(s), \\ T &= \sum_{j=0}^N \epsilon^{2j} T_{2j}, & P &= \sum_{j=0}^N \epsilon^{2j} P_{2j}. \end{aligned}$$

The coefficients of odd powers of ϵ in P and T vanish owing to the invariance of the system under rotations by half a wavelength. Substituting these expansions into (3) and the equations for x and y leads, at $\mathcal{O}(\epsilon)$, to

$$\mathcal{L}[\phi_1, x_1, y_1] \equiv \partial_s^3 \phi_1 + \left(\frac{3}{2} - T_0 \right) \partial_s \phi_1 - \ell^5 (x_1 x_0 + y_1 y_0) = 0.$$

To eliminate x_1 and y_1 , we compute $(\partial_s^2 \mathcal{L} + \mathcal{L})[\phi_1, x_1, y_1]$:

$$\partial_s^5 \phi_1 + \left(2 + P_0 + \frac{\ell^5}{2} \right) \partial_s^3 \phi_1 + \left(1 + P_0 + \frac{3\ell^5}{2} \right) \partial_s \phi_1 = 0.$$

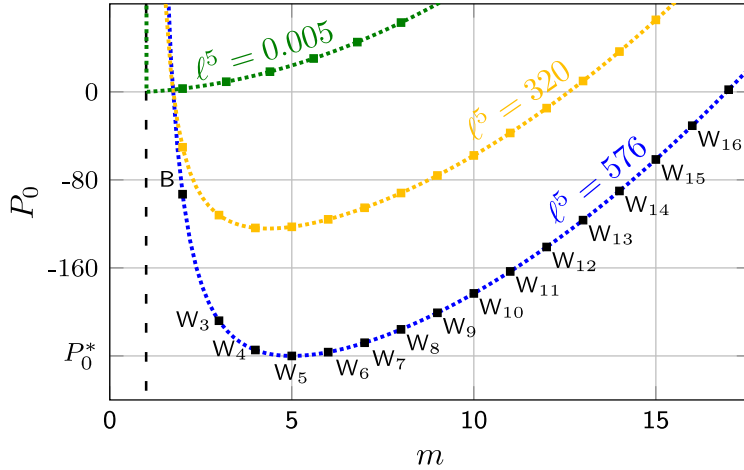


Figure 2. The wrinkle wavenumber m as a function of the pressure P_0 for $\ell^5 = 576$ (blue curve, $m^* = 5$), $\ell^5 = 320$ (yellow curve, $m^* = 4$) and $\ell^5 = 0.005$ (green curve, $m^* = 2$).

This equation reduces to an algebraic equation for the wavenumber m on assuming that $\phi_1(s) \propto \sin(ms + \delta)$:

$$m^5 - \left(2 + P_0 + \frac{\ell^5}{2}\right) m^3 + \left(1 + P_0 + \frac{3\ell^5}{2}\right) m = 0. \quad (8)$$

Modes with $m = 0$ (axisymmetric expansion) and $m = 1$ (translations) are excluded by inextensibility and pinning, respectively. Thus $m \geq 2$ and solutions with integers m correspond to periodic states we refer to as wrinkles (W_m); δ corresponds to a rigid rotation of the solution, and can be set to zero. Thus

$$\phi_1 = \sin(ms), \quad (9)$$

$$x_1 + iy_1 = \frac{m \cos(ms) - i \sin(ms)}{m^2 - 1} \exp(is). \quad (10)$$

Equation (8) is an important expression as it can be used to determine the critical pressure P_0^* for the onset of the wrinkling instability as the pressure increases and the wavenumber $m = m^*$ of the resulting wrinkles for a given ℓ . Figure 2 depicts P_0 as a function of m for three different ℓ values. The figure shows how the circular tube becomes wrinkled as P_0 overcomes the threshold $P_0^* \equiv (-\ell^5 + 4\ell^{5/2})/2$ and the interior depressurises. It also shows how the choice of ℓ determines the order of appearance of new unstable wavenumbers. A simple formula gives the critical wavenumber at P_0^* : $m^* = \sqrt{1 + \sqrt{\ell^5}}$. When $\ell^5 < 9$ the onset wavenumber is $m^* = 2$ since $m = 1$ corresponds to translations (figure 2).

In terms of physical parameters,

$$P_0^* = \frac{1}{2}K(r_0^2 - R^2) + 2\left(\frac{\mathcal{B}K}{R}\right)^{1/2}, \quad (11)$$

providing a key formula relating the critical pressure P_0^* for the onset of wrinkling to the geometry of the tube and the physical properties of the substrate and the lining. Expression (11) also indicates that the critical pressure can be tuned by a proper choice of r_0 and R , for instance, to generate lining wrinkles at pressure

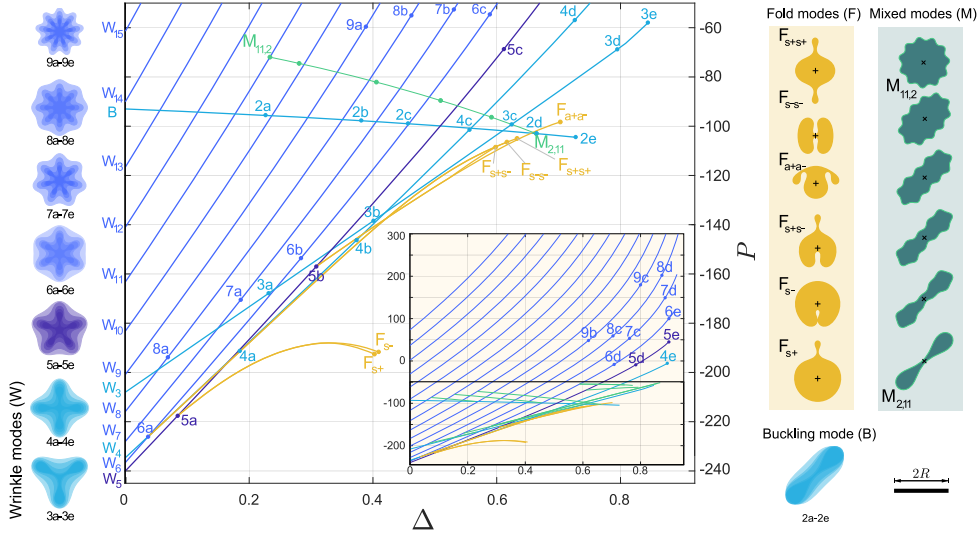


Figure 3. Bifurcation diagram for $\ell^5 = 576$ (corresponding to $m^* = 5$) showing the compression Δ as a function of the pressure P . The unperturbed circle state corresponds to $\Delta = 0$; the primary branch W_5 corresponding to states with wavenumber $m = 5$ is shown as a thin purple line. Subsequent primary wrinkle solutions W_m are labelled by their wavenumber ($m < 5$, cyan; $m > 5$, blue), while the secondary solutions are labelled F or M according to their type (fold or mixed mode). Branches are presented up to the point of self-contact. Sample solutions at the locations indicated in the main plot are shown alongside with the different wrinkle profiles for each m superposed. All solutions are reflected across the x axis for ease of visualization (solutions F and M have been rotated by 90° and 45° for convenience; the $+/\times$ symbols at the center of each profile indicate the orientation of the axes). The mixed mode branches extend between M_{m_1, m_2} where the first subscript indicates the primary wavenumber and the second the new wavenumber introduced at the secondary bifurcation. The subscripts \pm on F refer to the folded states with an extrusion (+) or intrusion (-). The subscripts s and a indicate whether these protrusions occur on the axis or off it. The letter B labels the buckling mode $m = 2$. A scale bar of unit length is included on the right. The inset shows the same results but over a larger range of P .

equilibrium ($P_0 = 0$). As mentioned, this requires $r_0 < R$, i.e. that the lining has an excess of length over the unlined tube inner perimeter. Likewise, for large ℓ , the critical wavelength of the wrinkles in terms of physical parameters simplifies to $\lambda^* = 2\pi R/m^* = 2\pi (\mathcal{B}/[KR])^{1/4}$, where KR can be identified with the foundation stiffness k if $R \approx r_0$.

We extend the above approach to compute periodic states with wavenumber m to higher order in ϵ (see Appendix B). We display the $\mathcal{O}(\epsilon^2)$ expressions for ϕ_2 , x_2 , y_2 , P_2 and T_2 below:

$$\begin{aligned} \phi_2 &= \frac{1}{8m} \sin(2ms), \\ x_2 + iy_2 &= \left[-\frac{1}{4} + \frac{i}{8m} \sin(2ms) \right] \exp(is), \\ P_2 &= \frac{2m^4 - 9m^2 + 3}{8(m^2 - 1)^2} \ell^5 + \frac{3(m^2 - 1)}{8}, \end{aligned}$$

$$T_2 = \frac{3}{8(m^2 - 1)}\ell^5 + \frac{3(m^2 + 1)}{8}.$$

We computed the expansion to $\mathcal{O}(\epsilon^7)$ using computer algebra. From these results, we can compute the slope $\partial P/\partial T$ of the primary wrinkle branches at the bifurcation points given by (8). This slope is always positive unless $m = 2$ and $\ell^5 \geq 81$. The mode $m = 2$ is special, because of its maximum wavelength; this mode is the first one to emerge in the absence of the intrinsic scale ℓ [30], and we therefore refer to it as the buckling mode (B).

In the following we extend the above results using numerical continuation and consider two cases. In the first (Section 4) substrate forces are substantial and wrinkling is present. In the second (Section 5) these forces are much weaker, wrinkling is absent and only buckling remains.

4. Numerical continuation: $\ell^5 = 576$

To compute strongly nonlinear solutions, we implemented (3) as a boundary value problem in AUTO [31] (see Appendix C for details) and numerically continued different wrinkle states for a given ℓ starting from the circle branch satisfying (7). Each increment in P requires the solution of a nonlinear eigenvalue problem for the response T . The results show that the weakly nonlinear theory is remarkably accurate, even when $\epsilon = \mathcal{O}(1)$ (see Appendix C for a comparison up to $\mathcal{O}(\epsilon^7)$ when $\ell^5 = 576$). The continuation approach also allows the computation of secondary branches of mixed modes (M) and folds (F).

Figure 3 shows the compression Δ as a function of the imposed pressure difference P for primary wrinkle states W_m with different wavenumbers m , starting with W_5 corresponding to the onset wavenumber $m^* = 5$. The figure shows not only the pressure required to initiate collapse of the tube (corresponding to $\Delta = 0$) but also its subsequent response to quasistatic increase in P , i.e., the figure represents the *tube law* describing the mechanical response for different modes of instability for the chosen value $\ell^5 = 576$. Figure 4 shows another measure of the response of the system, the tension T , also as a function of P . The (P, T) formulation provides the natural framework for numerical continuation. Both figures also show a number of secondary branches (the mixed states M and the fold states F) that bifurcate from the W states at finite amplitude, together with sample solution profiles at the locations indicated in the figures. All our plots use the same convention (colours and symbols).

While the circle solution ($\Delta = 0$ in figure 3, black line in figure 4) exists for any pressure P , we observe primary branches W_m of wrinkle states with different integer wavenumbers m only above the critical pressure P_0^* . Wrinkle solutions with wavenumbers below m^* are interspersed with those above m^* ; the wavenumber of the former decreases as P increases until $m = 2$; thereafter only wrinkle solutions with wavenumbers above m^* are present and m increases monotonically with the pressure P . When m^* is not an integer, the primary instability corresponds to the integer m nearest to m^* provided $m^* \geq 2$. Figure 3 shows that the compression Δ is almost proportional to the applied pressure P for all the wrinkle modes, i.e., that the modulus $Y \equiv \partial P/\partial \Delta$ is approximately constant. Each W_m branch ultimately results in self-contact and at this point the continuation is terminated. Self-contact forces can be included as in [30, 33], see also [14, 34], but this has not been done here.

Besides wrinkle modes, numerical continuation reveals two types of secondary

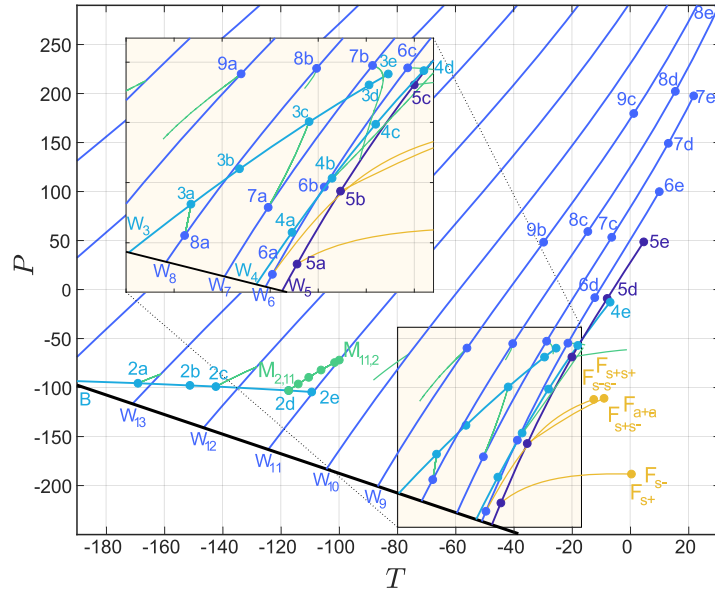


Figure 4. Bifurcation diagram for $\ell^5 = 576$ (corresponding to $m^* = 5$) showing the tension T resulting from an imposed pressure difference P following the same colour scheme and labels as in figure 3. The thick black line corresponds to the circle solution (7). The primary branch W_5 is shown as a thin purple line. The inset shows a zoom of the region near the primary bifurcation. The profiles corresponding to the labelled locations along each branch can be found in figure 3. An animation of the solutions along many of the solution branches in this figure is provided in the Supplementary Material [32].

branches. Most commonly, secondary branches connect a primary mode with $m \geq m^*$ to another primary mode with $m < m^*$. Figure 3 shows that all intermediate solutions along the mixed-mode branch connecting $m = 11$ and $m = 2$ primary branches, i.e. connecting the points $M_{11,2}$ to $M_{2,11}$, exhibit modulation at both wavenumbers. In fact, most of these interconnecting branches also result in self-contact, although longer, fully realisable interconnecting branches become possible as ℓ (and hence m^*) increases and the number of connections between W branches above and below m^* grows.

Secondary bifurcations that do not connect different primary modes are also present. These correspond to localised folds and come in pairs. The first pair $F_{s\pm}$ bifurcates from W_5 with F_{s+} representing a localised protrusion while F_{s-} represents localised invagination. Both branches reach self-contact at almost the same point (figures 3 and 4). A family F_a of asymmetric folds is also expected, but these states cannot be computed by AUTO with the imposed boundary conditions. Arrays of folds with different symmetries, analogous to those of [19], have also been found, with consistently higher degeneracy (see the yellow branches, e.g. F_{s+s-} in figures 3 and 4). Figure 3 also reveals that the modulus Y drops dramatically along the F branches, a well-known consequence of the appearance of folds. In the case of the M branches, the modulus Y can be negative as is the case for the buckling mode B .

We also examined the energy E of the different wrinkled, folded and buckled states as a function of the compression Δ . For small compression the lowest energy solution corresponds to $m^* = 5$, the natural wavenumber of the system for $\ell^5 = 576$,

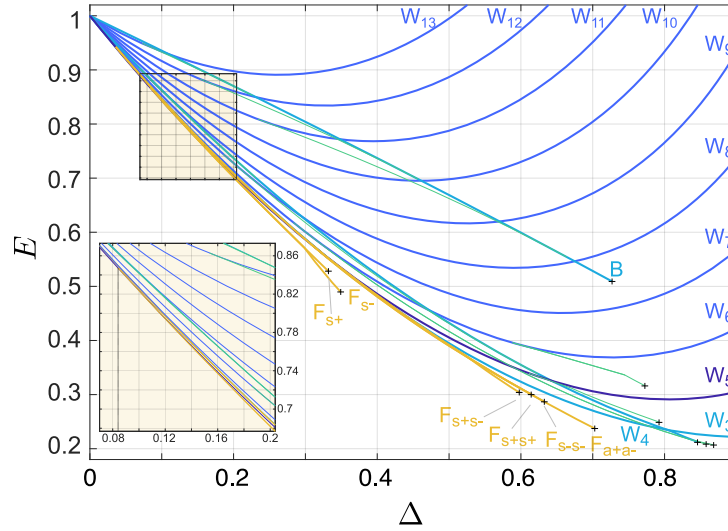


Figure 5. The energy E of the solutions in figures 3 and 4 across the full range of physical compression Δ . Points of self-contact are marked with crosses. All branches start from the circle solution at $\Delta = 0$. The inset shows a zoom of the region where the fold state F_{s+} becomes the global energy minimum.

as shown in figure 5. However, as the compression increases, the localised states $F_{s\pm}$ bifurcate from the $m^* = 5$ state, and the lowest energy state becomes F_{s+} , with F_{s-} at a slightly higher energy. This secondary bifurcation thus defines the wrinkle-to-fold transition, with threshold at $\Delta_c \approx 0.084$ for the particular case $\ell^5 = 576$. The direction of branching of F_{s+} and F_{s-} is consistent with that leading to spatially localised states in the bistable Swift-Hohenberg equation [35]. For higher compressions, the $F_{s\pm}$ are no longer realisable and other localised states correspond to global energy minima (figure 5).

Finally, in figure 6 we plot the maximum curvature of the different states we have studied. A rapid increase in maximum curvature can be observed along all wrinkle branches after their bifurcation from the constant curvature circle solution. Larger m values result in faster increase in κ_{\max} . Folds and some mixed states display even faster increase in curvature after they emerge from secondary bifurcations. The transition between the wrinkle state W_5 and the fold states $F_{s\pm}$, the first one to take place, occurs at $P = -217.7$ (figure 4) and corresponds to $\kappa_{\max} \approx 3.09$.

5. Numerical continuation: $\ell^5 = 0.005$

When $\ell = 0$ our problem becomes a pure buckling problem with no intrinsic length scale [30, 33]. In this case it is known that the first buckling mode corresponds to $m = 2$ with more complex buckling modes requiring larger and larger pressures as the wavenumber m increases. Moreover, in this regime the governing equation involves the curvature κ only and the problem is analytically solvable [36, 37, 38].

To confirm that our model possesses the correct limiting behaviour and thereby validate our numerical continuation approach we take ℓ^5 to be very small and compare our results with those for $\ell = 0$ and $\ell^5 = 576$. Specifically, we take $\ell^5 = 0.005$ and

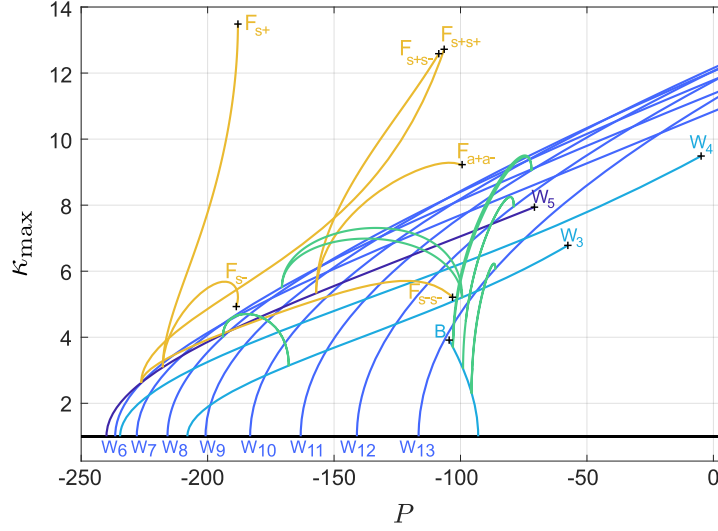


Figure 6. Maximum curvature κ_{\max} as a function of the pressure P across the full range of compression for $\ell^5 = 576$. Self-contact of the solutions is marked with crosses. The black horizontal line shows the $R = 1$ circle solution with $\kappa_{\max} \equiv 1$.

document the corresponding nonlinear results in Figure 7 for comparison with figures 3–6.

As expected, the first solution to emerge from the circle when $\ell^5 = 0.005$ is $m = 2$, i.e., the buckling mode B, and the wavenumber of the subsequent solutions that emerge increases monotonically with the pressure difference P . Moreover, the appearance of these states requires positive values of P and the corresponding branches all behave in a similar fashion. These solutions are thus the expected buckled states. In figure 7 these states are still labelled W but this is only because ℓ is not identically zero. For these small values of ℓ there are no mixed modes or folds prior to self-contact. In fact, such secondary bifurcations move farther and farther out along each primary branch and beyond the point of self-contact as $\ell^5 \rightarrow 0$, and conversely, down each primary branch and towards the circle solution when ℓ^5 increases. This process leads, for sufficiently large ℓ , to the appearance of secondary bifurcations prior to self-contact and for negative values of P , as in figure 4.

Figure 7a shows the compression Δ as a function of P for $\ell^5 = 0.005$ for comparison with figure 3 while figure 7b shows the tension T , also as a function of P . Figure 7a reveals that for smaller values of ℓ^5 the compression increases much more rapidly with P than for larger values ℓ^5 , a consequence of the absence of the stiffening effect of the substrate. These results are corroborated in 7b. The results in both figures are in accord with the weakly nonlinear theory: the modulus $Y = \partial P / \partial \Delta$ is now positive for all wavenumbers m (figure 7a) and likewise all primary branches have positive slopes $\partial P / \partial T$ (figure 7b), even for $m = 2$, as predicted by the theory.

Figure 7c shows the energy E as a function of the compression Δ for $\ell^5 = 0.005$ for comparison with figure 5. In contrast to the latter, E is now a monotonically increasing function of Δ and the wavenumber m : for small ℓ^5 the bending energy dominates the substrate energy and its contribution grows with increasing compression. Thus the

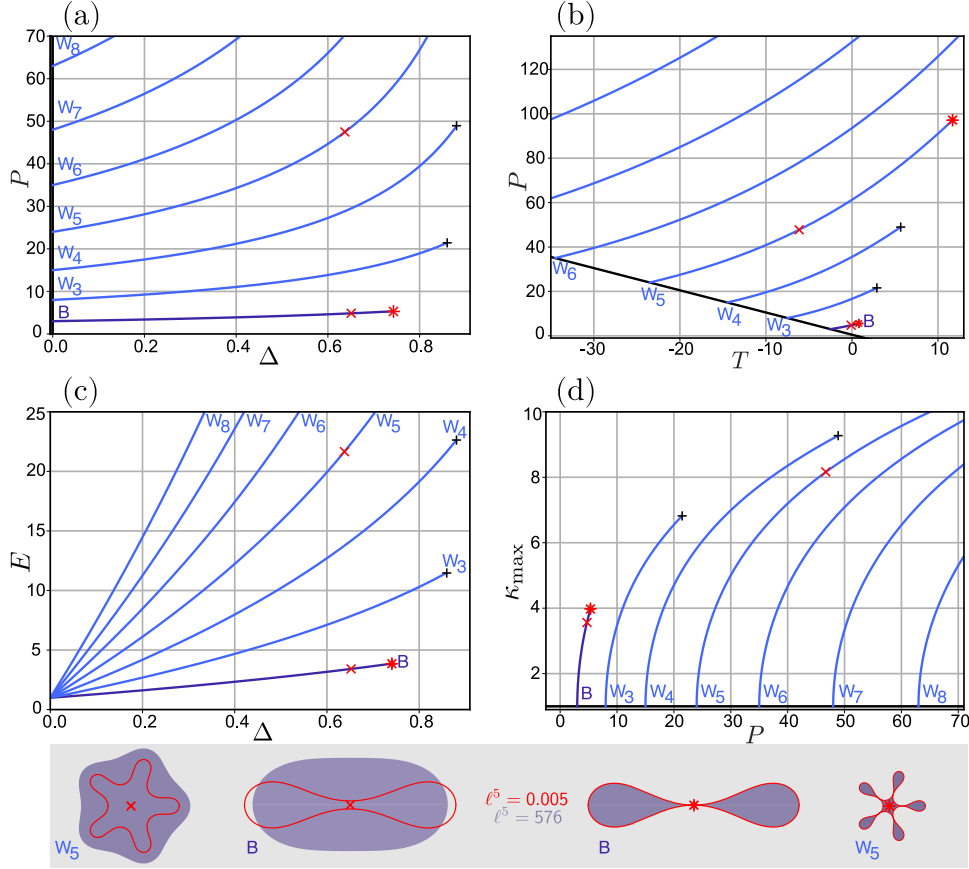


Figure 7. Bifurcation diagrams for $\ell^5 = 0.005$ for comparison with the case $\ell^5 = 576$ (figures 3–6) showing the circle state in black and all bifurcations from it, following the same colour scheme and labels as in figure 3. The first primary branch is now the $m = 2$ buckling mode (B, thin purple line). Solution branches are shown up to the point of self-contact (crosses). (a) The compression Δ as a function of the pressure P . The modulus $Y = \partial P / \partial \Delta$ is much smaller than in figure 3, but positive for all wavenumbers m including $m = 2$. (b) The tension T resulting from an imposed pressure difference P . All primary branches have positive slope $\partial P / \partial T$ in accord with the weakly nonlinear theory. (c) The energy E as a function of the compression Δ . The energy increases with increasing Δ for all primary branches until self-contact; the $m = 2$ buckled state (B, thin purple line) is the global minimum energy state. (d) The maximum curvature κ_{\max} as a function of P . The circle solution corresponds to $\kappa_{\max} = 1$ (black horizontal line). Self-contact is reached for much smaller pressure changes than for $\ell^5 = 576$. The bottom two panels depict the $m = 2$ and $m = 5$ solution profiles when P is increased from P_0 by 10% ($\Delta P = 24$, $\ell^5 = 576$) and 2% ($|\Delta P| = 1.86$, $\ell^5 = 0.005$). This point is indicated by a red \times in the figure: the tube is substantially more compressed when ℓ^5 is smaller. We also depict the $m = 2$ and $m = 5$ solutions overlaid at the point of self-contact for both ℓ values (red $*$, the only point at which different ℓ values can be precisely compared). The figure shows that for both $m = 2$ and $m = 5$ the profiles at this point are identical, i.e., the profiles at the point of contact are independent of ℓ .

lowest energy state at a given compression is that with the lowest overall curvature, i.e., the wavenumber $m = 2$ state is the minimum energy state and so is stable until self-contact (cross). After this point, stability is transferred to the next lowest wavenumber solution, $m = 3$, etc.

In figure 7d, we plot the maximum curvature as a function of P for comparison with figure 6. The figure shows that for small ℓ^5 maximum curvature is reached much earlier as P increases than for larger ℓ^5 . However, in each case, the maximum value of κ_{\max} necessarily coincides with the point of self-contact and is identical to the corresponding curvature when $\ell = 576$, i.e., κ_{\max} is independent of ℓ (figure 7, bottom right panel).

All this is in substantial contrast to the behaviour identified at larger ℓ^5 described in figures 3–6 but confirms that the solutions of (1) converge to the correct pure buckling limit as $\ell \rightarrow 0$.

Finally, the two lowest panels in figure 7 compare the profiles of the $m = 2$ and $m = 5$ solutions for the two different values of ℓ considered in this work. The comparison is made at a point 10% from the critical pressure P_0 for $m = 5$ and 2% from the critical pressure for $m = 2$ and again at the point of self-contact for both (red \times and $*$ symbols, respectively). We see that when ℓ is large the amount of compression for given ΔP is substantially less than for smaller ℓ . Thus the wrinkling or buckling process occurs over a smaller interval of P as ℓ decreases. However, at the point of self-contact the profiles in the two cases are identical and independent of the parameter ℓ as suggested by the weakly nonlinear analysis.

Evidently, as ℓ^5 decreases and the influence of the substrate wanes the bifurcation diagrams simplify dramatically and in the absence of the second length scale the system approaches the corresponding result for the unsupported ring ($\ell = 0$). This simplification arises because the secondary branches leading to both mixed modes and the folded states move past the point of self-contact thereby ceasing to be realisable. In this case the first primary mode is the lowest wavenumber mode, $m = 2$. Subsequent primary modes now come in monotonically with increasing m and all behave in a similar fashion. However, despite these changes the primary branches continue to bifurcate subcritically, in the sense that the lining loosens (tension T becomes less negative), as P increases.

On the other hand when ℓ^5 increases the wavenumber m^* of the mode that first sets in also increases (figure 2). This fact leads to repeated *mode jumping*. For example, $m^* = 4$ for $\ell^5 = 320$ while $m^* = 5$ for $\ell^5 = 576$. Thus the mode $m^* = 4$ remains dominant only over a finite interval of ℓ^5 , and as ℓ^5 increases $m^* = 4$ is replaced by a new dominant mode, $m^* = 5$. This transition is associated with a so-called codimension-two point where the dispersion relation (8) is simultaneously solved by two adjacent values of m , here $m^* = 4$ and $m^* = 5$. A similar situation occurs in the planar case, as described in detail in [19, Figure 5]. In particular, when $m^* = 4$ the folds F bifurcate from W_4 ; as ℓ^5 increases towards the codimension-two point $\ell_{4,5}^5 = 360$ the secondary bifurcations leading to the folds move down along the W_4 branch and reach zero amplitude when $\ell^5 = \ell_{4,5}^5$. For $\ell^5 > \ell_{4,5}^5$ the dominant mode is $m^* = 5$ and the secondary bifurcation to the fold state now takes place on W_5 . As ℓ^5 increases this bifurcation moves up along W_5 to a maximum amplitude before moving down again as the next codimension-two point is approached. This process repeats as ℓ^5 continues to increase, and Δ_c , the threshold for the onset of the fold state, therefore both oscillates and jumps from branch to branch. This behaviour is shown in figure 8(a) and is similar to that found in the planar case [19, Figure 5];

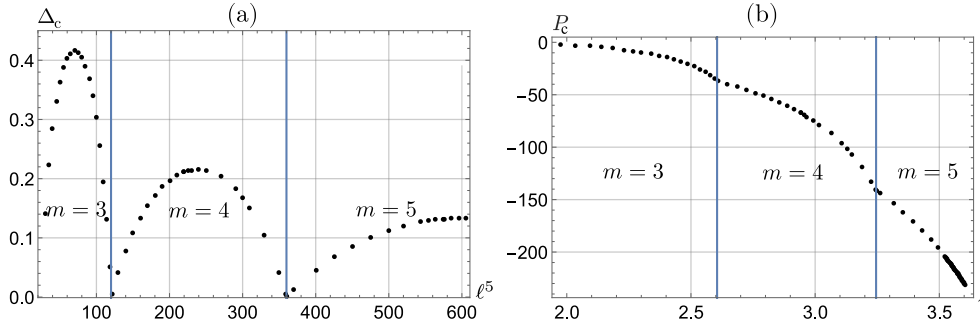


Figure 8. (a) The compression Δ_c at the secondary bifurcation from the primary wrinkled state to the first fold state as a function of ℓ^5 , showing the behaviour of this bifurcation point with changing wavenumber of the wrinkled state. The vertical lines show the codimension-two points $\ell_{m,m+1}^5 \equiv (m-1)m(m+1)(m+2)$ when $m = 3$ and 4. (b) The corresponding plot of P_c as a function of ℓ .

we expect that the tube problem studied here approaches the planar case once ℓ^5 is sufficiently large (sufficiently large tube radius).

6. Conclusion

In this article, we provided a simple model of an inextensible elastic lining of an inner-lined tube subjected to an imposed pressure difference, and described its buckled, wrinkled and folded solutions. We showed that wrinkling is statically generated by a competition between bending, soft-substrate forces and the applied pressure, and explored the limiting behaviour of our model as the strength of the substrate support is reduced eliminating the possibility of wrinkling. We showed that for sufficiently strong substrate support, increasing the applied pressure leads not only to a wrinkle-to-fold transition, but also to mixed states. The energies of these states were calculated using weakly nonlinear theory and by numerical continuation for strongly nonlinear solutions. The wrinkle state with wavelength closest to natural is initially the state with the least energy and is thus stable until a single-fold state bifurcates from it. As ℓ^5 increases, additional mixed modes arise prior to self-contact, and states with an increasing number of localised folds become possible. The solution profiles match well with observations and resemble structures in growing composite rings [7]. Our approach explains how the wavelength and amplitude of the wrinkles are selected as a function of parameters in pressure-driven wrinkling systems. This is in turn key to understanding, for example, the artery self-cleaning process arising from wrinkled-to-unwrinkled cycles triggered by blood pressure changes [20, 21] and can be a good starting point for more refined models that include adhesion. A natural question that arises is how the bending modulus, the size of the system and the substrate properties may be optimised to maximise in-plane curvature, thereby optimising the self-cleaning properties for a given pressure jump, while avoiding the wrinkle-to-fold transition. For weaker substrate support the first primary bifurcation is to the $m = 2$ buckling mode, and the secondary bifurcations move to large amplitudes, beyond the point of self-contact. Thus all bifurcation diagrams simplify and wavenumber of the primary branches increases monotonically with increasing pressure.

Applications of this work to the time-dependent artery problem and to other

systems exhibiting competition between buckling, wrinkling and folding will be described elsewhere.

Acknowledgments

This work was supported in part by the National Science Foundation under grant DMS-1908891 (BF, NV & EK). The work of NV was funded by the National Agency for Research and Development (ANID) through the Scholarship Program: Becas de Postdoctorado en el Extranjero, Becas Chile 2018 No. 74190030. LG was funded by grant Conicyt Fondecyt Iniciación 11170700. We thank E. Cerda for valuable discussions.

Appendix A. Derivation from Kirchhoff equations

In equilibrium, the forces acting on an element of the lining can be expressed in terms of the static Kirchhoff equations [12, 39]:

$$\partial_s \mathbf{F} + \left[P - \frac{1}{2} K (r_0^2 - r^2) \right] \mathbf{n} = 0, \quad (\text{A.1})$$

$$\partial_s \mathbf{M} + \mathbf{t} \times \mathbf{F} = 0, \quad (\text{A.2})$$

where \mathbf{F} and \mathbf{M} are the force and moment acting on the centerline of the element. The extra pressure in square brackets in (A.1) is due to the force per unit of area exerted by the substrate, modelled by a Winkler foundation [26] with a nonlinear quadratic term.

The moment is related to the local curvature of the ring by the constitutive relation $\mathbf{M} = (\mathcal{B} \partial_s \phi) \mathbf{k}$, where ϕ is the angle between a tangent to the ring and fixed horizontal axis, and \mathbf{k} is normal to the plane. Thus $\partial_s \mathbf{r} = (\cos \phi, \sin \phi)$. The unit vectors \mathbf{t} and \mathbf{n} are given by $\mathbf{t} = \partial_s \mathbf{r} = (\cos \phi, \sin \phi)$ and $\mathbf{n} = (-\sin \phi, \cos \phi)$; \mathbf{n} points towards the interior of the enclosed region. Accordingly, the system can be written in terms of five differential equations:

$$\begin{aligned} \partial_s x &= \cos \phi, \\ \partial_s y &= \sin \phi, \\ \mathcal{B} \partial_{ss} \phi &= F_x \sin \phi - F_y \cos \phi, \\ \partial_s F_x &= + \left[P - \frac{1}{2} K (r_0^2 - r^2) \right] \sin \phi, \\ \partial_s F_y &= - \left[P - \frac{1}{2} K (r_0^2 - r^2) \right] \cos \phi. \end{aligned}$$

The problem is defined after imposing the closed-curve boundary condition $\phi(L, t) = \phi(0, t) + 2\pi$, $L = 2\pi R$, and periodic boundary conditions on $\partial_s \phi, x, y, F_x$ and F_y . We show that this system of equations is equivalent to (3) of the text. For this purpose, we rewrite (A.2) using the constitutive relation $\mathbf{M} = (\mathcal{B} \partial_s \phi) \mathbf{k}$ and the identity $(\partial_s \phi) \mathbf{k} = \partial_s \mathbf{r} \times \partial_{ss} \mathbf{r}$,

$$\partial_s \mathbf{r} \times (\mathcal{B} \partial_{sss} \mathbf{r} + \mathbf{F}) = 0,$$

which is solved by $\mathbf{F} = -\mathcal{B} \partial_{sss} \mathbf{r} + \lambda \partial_s \mathbf{r}$, where we have introduced the Lagrange multiplier $\lambda(s)$ to incorporate inextensibility. The latter expression, substituted in

(A.1), yields

$$-\mathcal{B}\partial_{sss}\mathbf{r} + \lambda\partial_{ss}\mathbf{r} + \partial_s\lambda\partial_s\mathbf{r} + \left[P - \frac{1}{2}K(r_0^2 - r^2) \right] \mathbf{n} = 0.$$

To simplify this expression, we use the following identities: $\partial_s\mathbf{t} = (\partial_s\phi)\mathbf{n}$, $\partial_s\mathbf{n} = -(\partial_s\phi)\mathbf{t}$, $\partial_s\mathbf{r} = \mathbf{t}$, $\partial_{ss}\mathbf{r} = (\partial_s\phi)\mathbf{n}$, $\partial_{sss}\mathbf{r} = (\partial_{ss}\phi)\mathbf{n} - (\partial_s\phi)^2\mathbf{t}$ and $\partial_{ssss}\mathbf{r} = (\partial_{ssss}\phi - [\partial_s\phi]^3)\mathbf{n} - (3\partial_s\phi\partial_{ss}\phi)\mathbf{t}$. The result is

$$\begin{aligned} & \left(-\mathcal{B}\partial_{sss}\phi + \mathcal{B}[\partial_s\phi]^3 + \lambda\partial_s\phi + P - \frac{1}{2}K(r_0^2 - r^2) \right) \mathbf{n} + \dots \\ & \dots \left(3\partial_s\phi\partial_{ss}\phi + \partial_s\lambda \right) \mathbf{t} = 0. \end{aligned}$$

Since \mathbf{n} and \mathbf{t} form an orthonormal basis, the two terms in parentheses must both vanish. From the second, we obtain a differential equation for λ whose solution is

$$\lambda(s) = -\frac{3}{2}(\partial_s\phi)^2 + T,$$

where T is a constant. Replacing $\lambda(s)$ in the first set of parentheses by the above expression, we finally obtain:

$$-\mathcal{B}\partial_{sss}\phi - \frac{1}{2}B(\partial_s\phi)^3 + T\partial_s\phi + P - \frac{1}{2}K(r_0^2 - r^2) = 0, \quad (\text{A.3})$$

leading to eq. (3).

The same equation can also be derived from a constrained Lagrangian as done for the planar elastic sheet in [16].

Appendix B. Weakly nonlinear analysis

At each order in the weakly nonlinear analysis, we obtain a linear problem of the form

$$\mathcal{L}[\phi_j, x_j, y_j] \equiv \partial_s^3\phi_j + \left(\frac{3}{2} - T_0 \right) \partial_s\phi_j - \ell^5(x_0x_j + y_0y_j) = \mathcal{N}_j,$$

for $j = 1, 2, \dots$, with the first three \mathcal{N}_j given by

$$\begin{aligned} \mathcal{N}_1 &= 0 \\ \mathcal{N}_2 &= - \left(\frac{3}{2}(\partial_s\phi_1)^2 + \frac{1}{2}\ell^5(x_1^2 + y_1^2) - P_2 - T_2 \right) \\ \mathcal{N}_3 &= - \left(\frac{1}{2}(\partial_s\phi_1)^3 + 3(\partial_s\phi_1)(\partial_s\phi_2) + \ell^5(x_1x_2 + y_1y_2) \right) + T_2\partial_s\phi_1. \end{aligned}$$

To eliminate x_j and y_j from $\mathcal{L}[\phi_j, x_j, y_j]$, we compute $(\partial_s^2\mathcal{L} + \mathcal{L})[\phi_j, x_j, y_j]$:

$$\begin{aligned} & \partial_s^5\phi_j + \left(\frac{5}{2} - T_0 \right) \partial_s^3\phi_j + \left(\frac{3}{2} - T_0 \right) \partial_s\phi_j + \dots \\ & \dots \ell^5 [2(\partial_sx_0)(\partial_sx_j) + 2(\partial_sy_0)(\partial_sy_j) + x_0\partial_s^2x_j + y_0\partial_s^2y_j] = (\partial_s^2 + 1)\mathcal{N}_j. \end{aligned}$$

Expansion of the geometric identities $\partial_sx = \cos\phi$ and $\partial_sy = \sin\phi$ now results in

$$\partial_s^5\phi_j + \left(\frac{5}{2} - T_0 \right) \partial_s^3\phi_j + \left(\frac{3}{2} - T_0 + \ell^5 \right) \partial_s\phi_j = \mathcal{G}_j + (\partial_s^2 + 1)\mathcal{N}_j, \quad (\text{B.1})$$

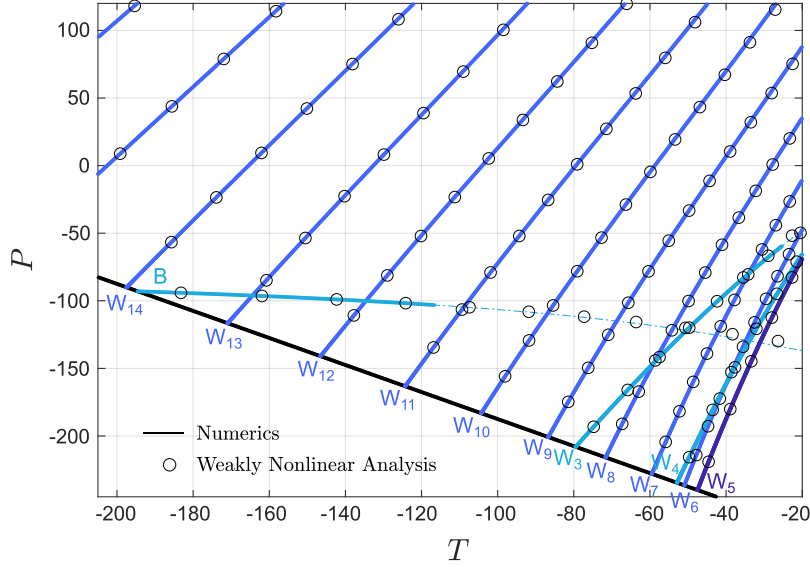


Figure B1. Comparison between numerical continuation for $\ell^5 = 576$ (solid lines) and the corresponding $\mathcal{O}(\epsilon^7)$ weakly nonlinear analysis (open circles) demonstrating excellent agreement between perturbation theory and numerically exact solutions extending to $\epsilon = \mathcal{O}(1)$ at the top of the figure (cf. figure C1 and Appendix D).

where the first three \mathcal{G}_j are given by

$$\begin{aligned}\mathcal{G}_1 &= 0 \\ \mathcal{G}_2 &= \frac{1}{2}\ell^5(\partial_s\phi_1)^2 \\ \mathcal{G}_3 &= \ell^5\left(\frac{1}{2}\phi_1^2\partial_s\phi_1 - \phi_1\phi_2\right).\end{aligned}$$

Solving (B.1) for $j = 1, 2$ subject to the requirement that the solution is periodic yields the expressions for ϕ_1, A_1 and for ϕ_2, A_2, P_2, T_2 given in the text. For j even, the solvability condition imposed on $\mathcal{G}_j + (\partial_s^2 + 1)\mathcal{N}_j$ generates $P_j(T_j)$, while for j odd, it generates $T_{j-1}(m, \ell^5)$. Higher order expressions were obtained through symbolic calculations using the software Maple.

Appendix C. Numerical continuation with AUTO

We implemented the problem (1) in AUTO [31] as a 5-dimensional boundary value problem on the domain $s \in [0, \pi]$, representing one half of the lining, with the boundary conditions $\phi(0) = \pi/2$, $\phi(\pi) = 3\pi/2$, $x(0) = x_0$, $x(\pi) = x_1$ and $y(0) = y(\pi) = 0$ together with the force-free conditions $\phi''(0) = \phi''(\pi) = 0$ [12]. The boundary conditions constrain the rotation symmetry in ϕ and eliminate translations in y , while the force-free boundary conditions permit reflection in $y = 0$ to generate solutions on the full circle. A 5-dimensional system with 8 boundary conditions requires 4 degrees of freedom in the parameters [40], so we perform our continuation in (P, T, x_0, x_1) .

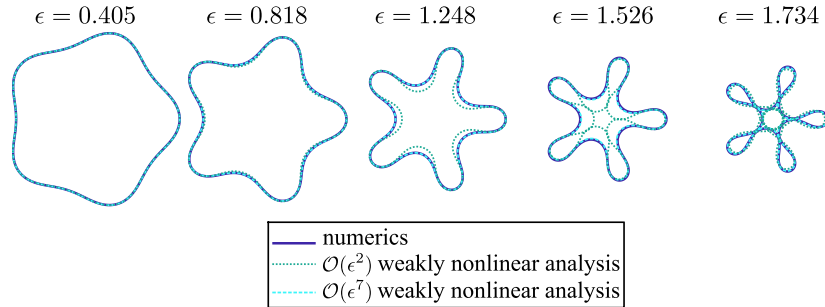


Figure C1. Comparison between numerical solutions on the W_5 branch and weakly nonlinear solutions at $\mathcal{O}(\epsilon^2)$ and $\mathcal{O}(\epsilon^7)$ when $l^5 = 576$.

This procedure allows T to adjust to increments in P and the endpoints x_1, x_2 to change in accordance with the zero-force condition. Figure 3 of the text shows the resulting full circle profiles.

The imposed boundary conditions prevent the computation of asymmetric states F_a that are also expected to appear via secondary bifurcations from wrinkled states.

Appendix D. Comparisons

In figure B1, we compare the results from numerical continuation of (3) of the text with the above boundary conditions and the corresponding results obtained above from weakly nonlinear theory carried out to $\mathcal{O}(\epsilon^7)$. The ϵ values corresponding to the maximum displayed extent of each branch are summarized in table D1. The results demonstrate excellent agreement between perturbation theory and the numerically exact solutions for $\epsilon \lesssim 1$. Equally good agreement is found for the solution profiles as shown in figure C1.

Table D1. Wavenumber m and maximum ϵ used in figure B1.

m	2	3	4	5	6	7	8	9	10	11	12	13	14
ϵ_{\max}	1.96	1.54	1.32	1.17	1.25	1.29	1.35	1.37	1.37	1.25	1.18	1.04	0.96

References

- [1] L. Pocivavsek, R. Dellsy, A. Kern, S. Johnson, B. Lin, K. Y. C. Lee, and E. Cerda. Stress and fold localization in thin elastic membranes. *Science*, 320:912–916, 2008.
- [2] F. Brau, P. Damman, H. Diamant, and T. A. Witten. Wrinkle to fold transition: influence of the substrate response. *Soft Matter*, 9:8177, 2013.
- [3] N. Stoop, R. Lagrange, D. Terwagne, P. M. Reis, and J. Dunkel. Curvature-induced symmetry breaking determines elastic surface patterns. *Nature Materials*, 14:337–342, 2015.
- [4] B. Roman and J. Bico. Elasto-capillarity: deforming an elastic structure with a liquid droplet. *J. Phys.: Condens. Matter*, 22:493101, 2010.
- [5] H. King, R. D. Schroll, B. Davidovitch, and N. Menon. Elastic sheet on a liquid drop reveals wrinkling and crumpling as distinct symmetry-breaking instabilities. *PNAS*, 109:9716–9720, 2012.
- [6] F. Box, D. O’Kiely, O. Kodio, M. Inizan, A. A. Castrejón-Pita, and D. Vella. Dynamics of wrinkling in ultrathin elastic sheets. *PNAS*, 116:20875–20880, 2019.

- [7] T. C. T. Michaels, R. Kusters, and L. Mahadevan. Puckering and wrinkling in a growing composite ring. *Proc. R. Soc. A: Mathematical, Physical and Engineering Sciences*, 477:20200999, 2021.
- [8] G. A. Vliegthart and G. Gompper. Compression, crumpling and collapse of spherical shells and capsules. *New J. Phys.*, 13:045020, 2011.
- [9] J. Marthelot, P.-T. Brun, F. López Jiménez, and P. M. Reis. Reversible patterning of spherical shells through constrained buckling. *Phys. Rev. Materials*, 1:025601, 2017.
- [10] E. Katifori, S. Alben, and D. R. Nelson. Collapse and folding of pressurized rings in two dimensions. *Phys. Rev. E*, 79:056604, 2009.
- [11] F. Box, O. Kodio, D. O’Kiely, V. Cantelli, A. Goriely, and D. Vella. Dynamic buckling of an elastic ring in a soap film. *Phys. Rev. Lett.*, 124:198003, 2020.
- [12] O. Kodio, A. Goriely, and D. Vella. Dynamic buckling of an inextensible elastic ring: Linear and nonlinear analyses. *Phys. Rev. E*, 101:053002, 2020.
- [13] L. Giomi and L. Mahadevan. Minimal surfaces bounded by elastic lines. *Proc. R. Soc. A: Mathematical, Physical and Engineering Sciences*, 468:1851–1864, 2012.
- [14] A. L. Hazel and T. Mullin. On the buckling of elastic rings by external confinement. *Phil. Trans. R. Soc. A*, 375:20160227, 2017.
- [15] B. Audoly. Localized buckling of a floating elastica. *Phys. Rev. E*, 84:011605, 2011.
- [16] H. Diamant and T. A. Witten. Compression induced folding of a sheet: An integrable system. *Phys. Rev. Lett.*, 107:164302, 2011.
- [17] M. Rivetti. Non-symmetric localized fold of a floating sheet. *Comptes Rendus Mécanique*, 341:333–338, 2013.
- [18] O. Oshri, F. Brau, and H. Diamant. Wrinkles and folds in a fluid-supported sheet of finite size. *Phys. Rev. E*, 91:052408, 2015.
- [19] L. Gordillo and E. Knobloch. Fluid-supported elastic sheet under compression: Multifold solutions. *Phys. Rev. E*, 99:043001, 2019.
- [20] L. Pocivavsek, J. Pugar, R. O’Dea, S.-H. Ye, W. Wagner, E. Tzeng, S. Velankar, and E. Cerda. Topography-driven surface renewal. *Nature Phys.*, 14:948–953, 2018.
- [21] L. Pocivavsek, S.-H. Ye, J. Pugar, E. Tzeng, E. Cerda, S. Velankar, and W. R. Wagner. Active wrinkles to drive self-cleaning: A strategy for anti-thrombotic surfaces for vascular grafts. *Biomaterials*, 192:226–234, 2019.
- [22] Ll. Carrillo, F. X. Magdaleno, J. Casademunt, and J. Ortín. Experiments in a rotating Hele-Shaw cell. *Phys. Rev. E*, 54:6260–6267, 1996.
- [23] G. D. Carvalho, H. Gadêlha, and J. A. Miranda. Elastic fingering in rotating Hele-Shaw flows. *Phys. Rev. E*, 89:053019, 2014.
- [24] G. D. Carvalho, H. Gadêlha, and J. A. Miranda. Stationary patterns in centrifugally driven interfacial elastic fingering. *Phys. Rev. E*, 90:063009, 2014.
- [25] P. Kumar, C. Hajdu, Á. Tóth, and D. Horváth. Flow-driven surface instabilities of tubular chitosan hydrogel. *ChemPhysChem*, 22:488–492, 2021.
- [26] E. Winkler. *Die Lehre von der Elastizität und Festigkeit*. Prague: Dominicus, 1867.
- [27] N. Nguyen, N. Nath, L. Deseri, E. Tzeng, S. S. Velankar, and L. Pocivavsek. Wrinkling instabilities for biologically relevant fiber-reinforced composite materials with a case study of Neo-Hookean/Ogden-Gasser-Holzapfel bilayer. *Biomechanics and Modeling in Mechanobiology*, 19(6):2375–2395, 2020.
- [28] G. W. Hunt, H. M. Bold, and J. M. T. Thompson. Structural localization phenomena and the dynamical phase-space analogy. *Proc. R. Soc. Lond. A*, 425:245–267, 1989.
- [29] T. C. T. Michaels, R. Kusters, A. J. Dear, C. Storm, J. C. Weaver, and L. Mahadevan. Geometric localization in supported elastic struts. *Proc. R. Soc. A: Mathematical, Physical and Engineering Sciences*, 475:20190370, 2019.
- [30] J. E. Flaherty, J. B. Keller, and S. I. Rubinow. Post buckling behavior of elastic tubes and rings with opposite sides in contact. *SIAM J. Appl. Math.*, 23:446–455, 1972.
- [31] E. J. Doedel, A. R. Champneys, F. Dercole, T. Fairgrieve, Yu. Kuznetsov, B. Oldeman, R. Paffenroth, B. Sandstede, X. Wang, and C. Zhang. *AUTO-07P: Continuation and Bifurcation Software for Ordinary Differential Equations*, Concordia University, 2012.
- [32] See Supplementary Material at ...
- [33] J. E. Flaherty and J. B. Keller. Contact problems involving a buckled elastica. *SIAM J. Appl. Math.*, 24:215–225, 1973.
- [34] A. Pocheau and B. Roman. Uniqueness of solutions for constrained elastica. *Physica D*, 192:161–186, 2004.
- [35] J. Burke and E. Knobloch. Localized states in the generalized Swift-Hohenberg equation. *Phys. Rev. E*, 73:056211, 2006.

- [36] V. M. Vassilev, P. A. Djondjorov, and I. M. Mladenov. Cylindrical equilibrium shapes of fluid membranes. *J. Phys. A: Mathematical and Theoretical*, 41:435201, 2008.
- [37] G. Arreaga, R. Capovilla, C. Chryssomalakos, and J. Guven. Area-constrained planar elastica. *Phys. Rev. E*, 65:031801, 2002.
- [38] A. Guckenberger and S. Gekle. Theory and algorithms to compute Helfrich bending forces: a review. *J. Phys.: Condensed Matter*, 29:203001, 2017.
- [39] B. Audoly and Y. Pomeau. *Elasticity and Geometry*. Oxford: Oxford University Press, 2010.
- [40] E. J. Doedel, H. B. Keller, and J. P. Kernevez. Numerical analysis and control of bifurcation problems. (II) Bifurcations in infinite dimensions. *International Journal of Bifurcation and Chaos*, 1:745–772, 1991.